

# We are IntechOpen, the world's leading publisher of Open Access books Built by scientists, for scientists

6,900

Open access books available

186,000

International authors and editors

200M

Downloads

Our authors are among the

154

Countries delivered to

TOP 1%

most cited scientists

12.2%

Contributors from top 500 universities



WEB OF SCIENCE™

Selection of our books indexed in the Book Citation Index  
in Web of Science™ Core Collection (BKCI)

Interested in publishing with us?  
Contact [book.department@intechopen.com](mailto:book.department@intechopen.com)

Numbers displayed above are based on latest data collected.  
For more information visit [www.intechopen.com](http://www.intechopen.com)



# First Principles Simulations on Surface Properties and Oxidation of Nitride Nuclear Fuels

Yuri Zhukovskii<sup>1</sup>, Dmitry Bocharov<sup>2,3</sup>,  
Denis Gryaznov<sup>1</sup> and Eugene Kotomin<sup>1</sup>

<sup>1</sup>*Institute of Solid State Physics,*

<sup>2</sup>*Faculty of Computing,*

<sup>3</sup>*Faculty of Physics and Mathematics, University of Latvia, Riga  
Latvia*

## 1. Introduction

Uranium mononitride (UN) is an advanced material for the non-oxide nuclear fuel considered as a promising candidate for the use in Generation-IV fast nuclear reactors to be in operation in the next 20-30 years [1, 2]. UN reveals several advantages over a traditional  $\text{UO}_2$ -type fuel (*e.g.*, higher thermal conductivity and metal density as well as high solubility in nitric acid in the case of fuel reprocessing [2]). However, one of important problems with actinide nitrides is their effective oxidation in oxygen-containing atmosphere which can affect nuclear fuel performance [3, 4]. Thus, it is important to understand the mechanism of the initial stage of UN oxidation and to find proper solutions, in order to improve in the future the fabrication process of this nuclear fuel.

In the present Chapter we acquire information on the atomic and electronic structure of both perfect and defective UN surfaces and discuss a mechanism of early stages of its surface oxidation. This Chapter is based on our own theoretical studies [5-10] as well as available theoretical and experimental literature.

## 2. Literature review

### 2.1 Experimental study of UN properties

Uranium mononitride is a metallic compound with low electrical resistivity ( $1.6 \cdot 10^{-4} \Omega \cdot \text{cm}$ ) [11], possessing *fcc* structure (space group  $Fm\bar{3}m$ , Fig. 1) over a wide temperature range [1]. The UN lattice constant is sensitive to carbon impurities [1] being insensitive to small oxygen impurities [12]. High melting temperature ( $\sim 2780 \pm 25$  K) [1], high fissile atom density ( $14.32 \text{ g/cm}^3$  vs  $10.96 \text{ g/cm}^3$  for  $\text{UO}_2$  [13]) and high thermal conductivity ( $13 \text{ W/mK}$ ) [14] make UN fuel a prospective material for nuclear reactors [1].

Fascinating and often enigmatic array of UN magnetic and electronic properties is induced by U(5f) electrons which are found to be intermediate between the highly localized 4f

electrons of the lanthanides and the strongly delocalized  $d$  valence electrons in the transition metals [15]. UN was found to be antiferromagnetic at temperatures below the Neel temperature ( $T_N \sim 53$  K), which was detected in the heat capacity measurements [1]. Investigation of the magnetic structure of UN was performed in 60s by means of neutron diffraction [11]. The magnetic structure known as ordering of the first kind, where ferromagnetic sheets parallel to the (001) planes are antiferromagnetically coupled, was deduced [11]. The value of  $0.75 \mu_B$  found for the magnetic moment of U at  $T < T_N$  appears to be surprisingly small (the lowest amongst the uranium mononitrides UX, where X = P, As, Sb) [11].

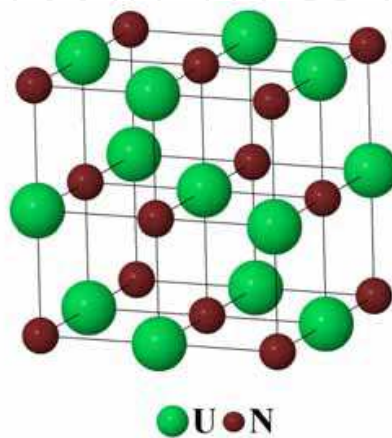


Fig. 1. An *fcc* structure of uranium mononitride.

Photoelectron spectroscopy also confirmed the complexity of UN. A very high density of states in proximity of the Fermi level was observed, which gives an evidence that the U(5*f*) electrons participate in bonding being strongly hybridized with the U(6*d*) electrons. The occupation of the conduction U(5*f*) band is  $2.2 \pm 0.5 e$ , of which  $\sim 1.8 e$  resides near the Fermi level [15]. In Ref. [16], the band structure of UN at 25 K was constructed taking into account the second derivative of high-resolution angle-resolved photoemission spectra. A highly dispersive band was observed for UN near the Fermi level centered at  $\Gamma(X)$  point, whose bottom is located at about 2 eV. First magneto-optical Kerr effect measurements on UN also showed narrow U(5*f*) band around the Fermi level as well as increased hybridization of the U(5*f*) states with U(6*d*) and N(2*p*) states as compared to similar data for heavier uranium mononitrides [17]. On the other hand, uranium nitride has the smallest U-U distance amongst the UX compounds (X=N, P, As, Sb, S, Se, and Te) which is equal to 3.46 Å being close to the critical 3.4 Å value given by Hill diagrams separating non-magnetic from magnetic compounds.

## 2.2 Interaction of uranium nitride with oxygen

The oxidation of uranium mononitride in an oxygen atmosphere was systematically studied in Ref. [18]. The two main types of UN samples were used in these experiments: powdered UN and smoothly polished UN pieces. Following a weight change of the UN powder sample during the oxidation process at elevated temperatures, a strong exothermic reaction was identified at 250°C characterized by rapid oxygen absorption. The weight was increased by 11.5%. The X-ray diffraction patterns of the intermediate product at temperatures 250-

260°C showed both weak diffraction lines corresponding to UN and very pronounced line broadening corresponding to  $\text{UO}_2$ . The polished UN pieces were used for kinetic study of UN oxidation. Measurements showed that the reaction rate is proportional to the area covered by the oxide or the oxidized volume. Analysis of both kinetic studies and X-ray diffraction data suggested that the isothermal oxidation of UN proceeds from the beginning of lateral spreading of the oxide,  $\text{UO}_2(\text{N})$ , accompanied by a slight  $\text{N}_2$  release and by the formation of  $\text{U}_2\text{N}_3(\text{O})$  during the reaction between UN and released nitrogen.

In Ref. [19], such characteristics as the chemical composition, phases, lattice parameter, sinterability, grain growth and thermal conductivity of the samples are investigated using chemical, X-ray and ceramographic analyses for pellets of uranium nitride powder containing certain amounts of oxygen (~0.3, ~0.6 and ~1.0 wt%) which are products of carbothermic reduction. Note, that conductivity of UN samples was found to be gradually decreasing under oxidation [20]. The principal results are that the average UN grain size of matrix phase decreases with increase of oxygen content. Moreover, thermal conductivity of the pellets containing about 1 wt% oxygen is lower than that of usual nitride pellets (containing 1000-2000 ppm oxygen) by 9-10% and 12-13% at 1000 and 1500 K, respectively.

In Ref. [21], direct ammonolysis of  $\text{UF}_4$  was used, to synthesize  $\text{UN}_2$  sample which was heated to 1100° C for 30 min inside the inert atmosphere producing these UN powder samples with  $\text{UO}_2$  inclusions saturated at 5.0 wt%. The observed characteristic length distribution of particles ranges from 0.1 to 6  $\mu\text{m}$ . The measured UN surface area was equal to 0.23  $\text{m}^2/\text{g}$ . Both the electron microprobes and X-ray diffraction analysis showed that there are considerable amount of oxygen impurities in UN samples consisting of the primary UN phase and the secondary  $\text{UO}_2$  impurity phase. This supports the conclusion that oxide impurities are likely to be formed by a diffusive process from the chemical environment and, thus, they are also likely to be formed along the particle surface. Concentration of oxygen impurities increases upon exposure to air: UN sample exposed for 3 months shows the growth of oxide contamination. The quantitative analysis performed for the XRD patterns showed that the  $\text{UO}_2$  concentration increases from 5.0 wt% to 14.8 wt% over this time period [21].

The UPS measurements performed for thin layers of  $\text{UO}_2$ , UN,  $\text{UO}_x\text{N}_y$  and  $\text{UO}_x\text{C}_y$  using He-II 40.81 eV excitation radiation produced by a UV rare-gas discharge source were described in [20, 22]. These layers were prepared *in situ* by reactive DC sputtering in an Ar atmosphere. Fig. 2 shows that U(5f) states form a peak close to the Fermi level (0 eV), which proves their itinerant character. The valence band spectrum of  $\text{UO}_x\text{N}_y$  shows a broad band interpreted as superposition of the narrow O(2p) and N(2p) bands. The maximum at 6 eV binding energy clearly comes from the O(2p) state contribution while the smaller shoulder at 3 eV coincides with the N(2p) signal in UN sample.

In Ref. [23], the XPS and XRD methods as well as the measurement of ammonia concentration in the aqueous phase at the end of each experiment were used, in order to study corrosion of UN in water.  $\text{UO}_2$  film arising during the surface reaction with water was detected using XPS for the surface of freshly polished UN pellet. The high corrosion rates of UN in water (at 928 °C) indicated that UN is not stable inside the hot aqueous environment. Corrosion rate for UN is much lower than that for U metal but higher that of uranium silicide.

Thickness, composition, concentration depth profile and ion irradiation effects on uranium nitride thin films deposited upon fused silica were investigated in [14] using Rutherford

Backscattering Spectroscopy (RBS) for 2 MeV He<sup>+</sup> ions. Deposition at -200 °C provided formation of thick stoichiometric UN film. This film was found to be stable for exposure to air. The surface oxidation is much more enhanced and the oxidized surface layer becomes gradually thicker in films deposited at higher temperature (+25 °C and +300 °C). A large influence of the ion irradiation on the film structure and layer composition was observed. This study also showed possibility to produce stoichiometric UN film with the required uranium content of 50% and to obtain the required film thickness by ion irradiation.

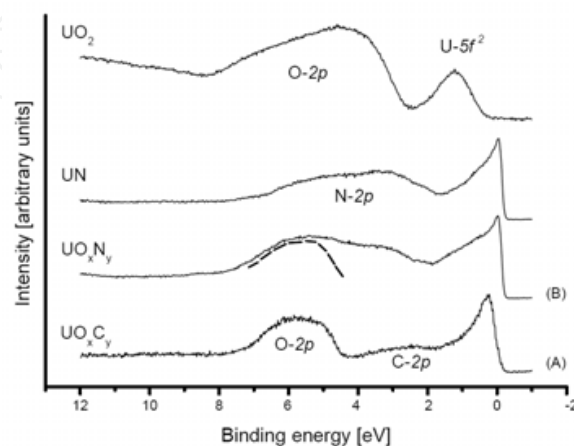


Fig. 2. He-II valence band spectra of  $UO_xC_y$ ,  $UO_xN_y$ , UN and  $UO_2$  spectra. Reproduced with permission from [22].

Finally, experimental studies also clearly showed that oxygen contacting to the surface of uranium mononitride can result in growth of the oxide compound and, at initial stages, can lead to the formation of surface layer structurally similar to oxynitrides  $UO_xN_y$  [24].

### 2.3 Previous theoretical simulations on UN

Due to increasing interest in the fast breeder reactors and to the issues of transmutation of uranium, plutonium and minor actinides, first-principles and other theoretical calculations on actinide nitride compounds attract great attention nowadays. However, previous theoretical studies were performed mainly on UN bulk. Beginning from 80s [25-27], the methods based on the DFT were often applied to actinide materials.

In first relativistic calculations on UN single crystal, methods of full-potential Korringa-Kohn-Rostoker (KKR) Green's function [25] and Linear Muffin-Tin Orbitals (LMTO) [26-27] were used, focused mainly on the atomic and electronic structure. The calculated lattice parameters were found within 3% of experimental value, whereas the bulk modulus was reproduced worse when comparing with experimental data: by 23% higher [26] or within 10% [27]. The analysis of density of states (DOS) showed no gap between the valence and conduction bands in UN. The valence bands, found to be ~5-6 eV wide, appeared at ~2 eV below the Fermi level. The main peak was located by 1 eV below the Fermi level [27].

Recently, the all-electron calculations within the Linear Augmented Plane Wave (LAPW) approach were performed, using the PBE (Perdew-Burke-Ernzerhof) exchange-correlation functional (with and without incorporation of the spin-orbital coupling) as implemented in the WIEN-2k program package, for a series of actinide nitrides (AcN, ThN, PaN, UN, NpN,

PuN, AmN) [28]. The formation enthalpies mainly determined by the ground state cohesive energies were evaluated. The formation enthalpies are in excellent agreement with the experimental data (in the case of UN, the best correlation can be achieved with the results of calorimetric measurements: theoretical value of  $-291.0 \text{ kJ}\cdot\text{mol}^{-1}$  vs. experimental value of  $-290.5\pm 1.4 \text{ kJ}\cdot\text{mol}^{-1}$  [29]). Some discrepancies between the experimental data and results of theoretical simulations for PuN and ThN still need to be clarified.

In Ref. [30], the same LAPW formalism within the GGA approximation was used to study the structural, electronic, and magnetic properties of the actinide compounds. The observed chemical bonding between the actinides and nitrogen was characterized by a significant ionic character. The calculated cohesive energies were found to be close to the experimental values ( $14.3 \text{ eV}$  vs.  $13.6 \text{ eV}$ , respectively). Although the lattice constant for UN was calculated in a good agreement with the experiment (within  $\sim 0.4\%$ ), it was found to be ferromagnetic (FM) that contradicts to experimental results. The calculated spin density for UN in FM state was equal to  $0.96 \mu_{\text{B}}$ . On the other hand, the calculated ferromagnetic structure of NpN and the non-magnetic structure of ThN agreed well with the corresponding experimental measurements.

In Ref. [31], the all-electron relativistic spin-polarized DFT calculations were performed, to evaluate the total energies, optimized geometries, as well as electronic and thermodynamic properties of perfect stoichiometric UN and UN<sub>2</sub> single crystals. For this purpose, the GGA Perdew-Wang (PW91) non-local exchange-correlation functional was used, and the numerical double- $\xi$  basis sets with  $d$ -type polarization functions were added to atoms heavier than hydrogen. Structural properties as measured using EXAFS and XRD methods were successfully reproduced in the calculations (within error of  $0.03 \text{ \AA}$ ). The DOS showed hybridization of the U( $6d$ ), U( $5f$ ) and N( $2p$ ) states as well as main contribution of  $5f$ -electrons to the conduction band. In this work the phonon frequencies and corresponding heat capacities were calculated. The authors suggested an important role of itinerant  $5f$  states in the thermodynamic properties.

The lattice parameters, electronic structure, as well as the thermodynamic properties of UN using LDA+ $U$  and GGA+ $U$  semi-empirical schemes and plane wave (PW) approach were presented in [32]. The total energy dependences on Hubbard  $U$ -parameter for UN bulk in FM and AFM states obtained in those calculations show that the FM state is preferable for the range of  $U$ -parameter between 0 and 2 eV while the AFM state could be favorable for  $U$ -parameter larger than 2 eV. Nevertheless, even though the AFM state of UN bulk is reproduced, the ground state is hardly obtainable when using the DFT+ $U$  method [33]. The value of  $U$ -parameter must be carefully suggested otherwise large errors may appear when calculating defect formation energies [34-35]. We avoid application of this method in the present study due to ferromagnetic nature of UN surface [36] reproducible by standard DFT functionals.

In other PW calculations on UN bulk, the VASP and CASTEP computer codes were employed using the PW91 exchange-correlation functional [37-38]. Both series of calculations agree well on the mixed metallic-covalent nature of UN chemical bonds reproducing the lattice constants, bulk moduli and cohesive energies.

The magnetic structure of UN was also addressed in Ref. [39]. In this study the so-called [111] magnetic structure was compared to the [001] one used here. Besides, the calculations

were done within the careful GGA+ $U$  study and did not reveal the energetic preference of the [111] magnetic structure except for very small values of Hubbard  $U$ -parameter.

Also, the PW approach combined with a supercell model was used for the calculations on defective UN crystal, containing single point defects as well as Frenkel and Schottky defect pairs. It was shown in Ref. [38] that the N-vacancies practically have no influence on the UN lattice constant, even for concentrations higher than 25%. The defect formation energies in the UN bulk were obtained to be equal 9.1-9.7 eV for the N-vacancy and 9.4-10.3 eV for the U-vacancy. The migration energy of the interstitial N-atom along the (001) axis was relatively low, i.e., 2.73 eV [37]. This fact confirms the suggestion that the interstitial migration might be a predominant mechanism of N-atom diffusion in the UN fuel [1]. Apart the behavior of empty vacancies, the O atom incorporation into vacancies in bulk UN was considered too [40]. Its incorporation into the N vacancies was found to be energetically more favorable as compared to the interstitial sites. However, the calculated values of solution energy showed an opposite effect. The calculated migration energy of the interstitial O atoms is very similar (2.84 eV). This fact confirms that the O atoms can easily substitute the host N atoms in UN structure.

### 3. Computational method

The UN (001) and (110) surfaces can be simulated using the symmetrical slabs containing odd number of atomic layers and separated by the vacuum gap of 38.9 Å corresponding, thus, to UN(001) 16 inter-layers. The vacuum gap is a property of plane wave approach. The suggested vacuum gaps are large enough to exclude the direct interaction between the neighboring two-dimensional (2D) slabs.

One should use the so-called supercell approach to simulate single point defects or an oxygen atom adsorbed/incorporated on/into the surface. Using  $2 \times 2$  and  $3 \times 3$  extensions of primitive unit cell, lateral interactions between the defects can be also estimated. Such supercells contain four ( $2 \times 2$ ) and nine ( $3 \times 3$ ) pairs of the N- and U-atoms in each defectless layer of the slab. Periodically distributed surface vacancies (or oxygen atoms/molecules) *per* surface unit cell correspond to point defect (oxygen) concentrations of 0.25 and 0.11 monolayers (ML), respectively.

The results of first-principles PW calculations as obtained using Vienna Ab-initio Simulation Package (VASP) [41-43] will be further discussed. The VASP code treats core electrons using pseudopotentials, whereas the semi-core electrons of U atoms and all the valence electrons are represented by PWs. The electronic structure is calculated within the projector augmented wave (PAW) method [44]. Details on how the computation parameters could be properly chosen in such computations are discussed elsewhere [43]. Here we would like to mention that the cut-off energy in the calculations was chosen 520 eV. The integrations in the reciprocal space of the Brillouin zone were performed with  $8 \times 8 \times 1$  and  $4 \times 4 \times 1$  Monkhorst-Pack [45] mesh for the (001) and (110) surfaces, respectively. All the calculations involved the FM state of the surface only and full relaxation of all degrees of freedom if not otherwise stated.

### 4. Defect-free UN (001) and (110) surfaces

According to Tasker's analysis [46] the (001) surface must have the lowest surface energy for the rock-salt compounds. However, one could suppose facets with different crystallographic

orientations for nano-particles and polycrystalline materials. Moreover, the role of different surfaces may be changed with the temperature. Therefore, additional calculations are also required for other surfaces to improve the validity of our results. In the present analysis we consider the (110) surface, for example. The (110) surface is characterized by smaller interlayer distances as compared to the (001) one. In this Chapter, the results of atomic oxygen adsorption, the formation of N-vacancies and oxygen atom incorporation, are discussed for the (110) surface and compared to those for the (001) surface.

The surface energy  $E_{surf}$  as a function of the number of layers in the layers is given in Table 1 for both the (001) and (110) defectless surfaces (also shown in Fig. 3). The surface energy is calculated according to

$$E_{surf}(n) = \frac{1}{2S}(E_n - nE_b) \quad (1)$$

where  $n$  the number of layers on the surface,  $S$  the surface unit cell area,  $E_n$  and  $E_b$  the total energy of the surface unit cell and bulk primitive unit cell, respectively. The importance of spin relaxation is also addressed here. The spin magnetic moment relaxation leads to considerable changes (Table 1) suggesting lower  $E_{surf}$  values and dependence on the number of layers in the slab. The lattice relaxation energies in spin-relaxed calculations turn out to be quite small, *i.e.*,  $\sim 0.03$  eV. Depending on the slab thickness,  $E_{surf}$  is  $\sim 0.5-0.7$  J m<sup>-2</sup> larger for the (110) surface as compared to the (001) one. This further supports the importance of the (001) surface for this study.

The atomic displacements  $\Delta z$  from perfect lattice sites differ significantly for the U atoms positioned at the surface and sub-surface layers (Table 2) being, however, somewhat larger for the 5-layer slab. The displacements of N atoms for all the slab thicknesses remain almost unchanged. Note that the N atoms on the (001) surface are displaced up whereas the U atoms are shifted inwards the slab center which results in the surface rumpling up to 1.2% of the lattice constant. In contrary, the surface U atoms of rumped (110) surface lie higher than the corresponding N atoms.

In the next section we show how the electronic structure changes with the presence of point defects on the surface. This analysis will include the DOS and electronic charge distributions for perfect and defective surfaces.

## 5. Modeling of single N and U vacancies

### 5.1 Model and formation energies

To understand the oxidation mechanism in more detail, one has to take into account *surface defects* and their interaction with oxygen. The calculation of not only the surface defects, but also of the sub-surface and the central layer defects in the slab is necessary. Since we have chosen symmetrical slabs, two defects appear in the system due to symmetry with respect to the central layer. Let us define the formation energy of a point defect as

$$E_{form}^{N(U)vac} = \frac{1}{2} \left( E^{UN(U/N_{vac})} + 2E_{ref-1(II)}^{N(U)} - E^{UN} \right), \quad (2a)$$

for the surface and sub-surface vacancies, or

$$E_{\text{form}}^{\text{N(U)vac}} = E^{\text{UN(U/N}_{\text{vac}})} + E_{\text{ref}_I}^{\text{N(U)}} - E^{\text{UN}}, \quad (2b)$$

for a vacancy in the central layer of the slab. Here  $E^{\text{UN(U/N}_{\text{vac}})}$  the total energy of fully relaxed slab containing either the N or U-vacancies,  $E^{\text{UN}}$  the same for a defect-free slab, while  $E_{\text{ref}_I}^{\text{N(U)}}$  is reference energy for the N (or U) atom.

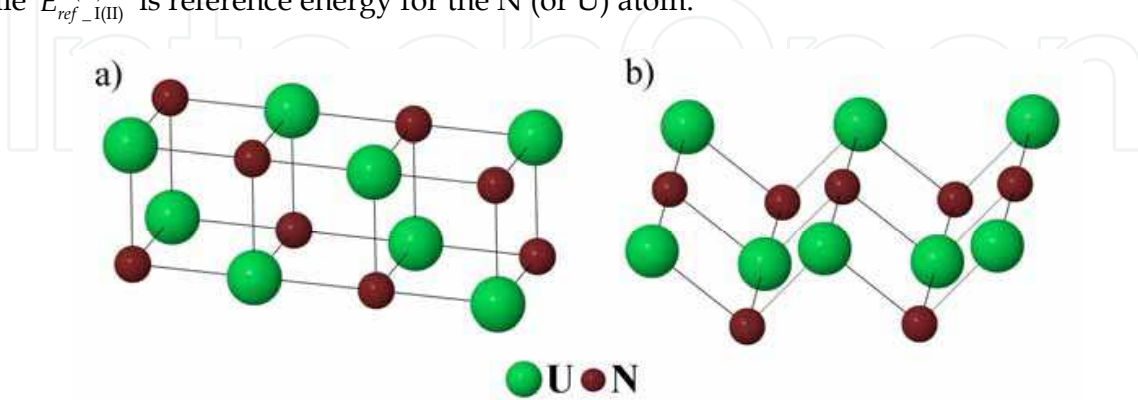


Fig. 3. The 2-layer model for the UN (001) (a) and (110) (b) surfaces.

Number of layers	$E_{\text{surf}}$ (J m <sup>-2</sup> ) spin-frozen slab (001)	$E_{\text{surf}}$ (J m <sup>-2</sup> ) spin-relaxed slab (001)	$E_{\text{surf}}$ (J m <sup>-2</sup> ) spin-relaxed slab (110)
5	1.69	1.44	1.977
7	1.70	1.37	1.928
9	1.70	1.29	1.878
11	1.69	1.22	1.830

Table 1. Surface energies  $E_{\text{surf}}$  (J m<sup>-2</sup>) for the defect-free UN (001) and (110) surfaces. In spin-frozen calculations, the spin magnetic moment of U atom was fixed at  $1\mu_{\text{B}}$

Two reference states for the calculations of the defect formation energy are often used in the literature which we would like to compare and discuss for our study. The first reference corresponds to the N(U) isolated atom in the triplet (quartet) spin state determined by  $2p^3$  ( $5f^36d^1$ ) valence electron configurations (hereafter, reference I in Table 3), *i.e.*,

$$E_{\text{ref}_I}^{\text{N(U)}} = E_{\text{atom}}^{\text{N(U)}}. \quad (3)$$

The isolated atom is calculated in a large rectangular parallelepiped box ( $28.28 \times 28.28 \times 22 \text{ \AA}^3$ ).

The second reference state (hereafter, reference II as in Table 3) represents the chemical potential of N (U) atom which is defined as a function of temperature and partial nitrogen pressure. By neglecting these effects, the N chemical potential can be treated as the energy of atom in the molecule  $\text{N}_2$  and thus considered at 0 K. Consequently, the chemical potential of U atom is given by the one-half total energy (*per* unit cell) of U single crystal in its low-temperature  $\alpha$ -phase having the orthorhombic structure [47]. The corresponding second reference energies can be estimated as:

$$E_{ref\_II}^N = \mu_{N_2} = \frac{1}{2} E_{tot} [N_2], \quad (3a)$$

$$E_{ref\_II}^U = \mu_{\alpha-U} = \frac{1}{2} E_{tot} [\alpha-U], \quad (3b)$$

where  $E_{tot}[N_2]$  is the total energy of nitrogen molecule while  $E_{tot}[\alpha-U]$  the total energy of U metal bulk unit cell containing two atoms. In accordance with *Eqs. 3* the chemical potentials of N and U represent extreme cases of N(U)-rich conditions [48], *i.e.*, their minimum values have not been considered in the present study. The formation energy of N- (U-) vacancy with respect to the  $N_2$  molecule (or  $\alpha-U$  single crystal) and the energy of N (U) isolated atom are closely related: the former being larger than the latter by half the binding energy of the  $N_2$  molecule or half the cohesive energy of  $\alpha-U$  single crystal.

Number of atomic planes	U				N			
	(001)		(110)		(001)		(110)	
	Surface	Sub-surface	Surface	Sub-surface	Surface	Sub-surface	Surface	Sub-surface
5	-0.050	-0.012	-0.053	-0.005	0.023	0.023	-0.279	0.068
7	-0.046	-0.009	-0.038	-0.009	0.024	0.028	-0.272	0.092
9	-0.047	-0.011	-0.042	-0.014	0.024	0.028	-0.279	0.091
11	-0.047	-0.011	-0.015	0.015	0.025	0.031	-0.252	0.118

\* negative sign means an inward atomic displacement towards the mirror plane of the slab

Table 2. Atomic displacements  $\Delta z(\text{\AA})^*$  for defect-free UN (001) and (110) surfaces.

The optimized lattice parameters of  $\alpha-U$  ( $a = 2.80 \text{ \AA}$ ,  $b = 5.88 \text{ \AA}$ ,  $c = 4.91 \text{ \AA}$ ) have been slightly underestimated as compared to values obtained experimentally [47] and calculated [49-50], except for the parameter  $b$  which is in a good agreement with experimental value of  $5.87 \text{ \AA}$  [47] (while  $a=2.86 \text{ \AA}$ ,  $c = 4.96 \text{ \AA}$  [47]). Also, the ratios  $c/a$ ,  $b/a$  as well as the parameter  $c$  are well verified by another plane-wave DFT study [51]. Analogously to an isolated nitrogen atom, the  $N_2$  molecule has been calculated in the cubic box but of a smaller size ( $8 \times 8 \times 8 \text{ \AA}^3$ ). The molecule  $N_2$  is characterized by the bond length of  $1.12 \text{ \AA}$  and the binding energy of  $10.63 \text{ eV}$  being well comparable with the experimental values of  $1.10 \text{ \AA}$  and  $9.80 \text{ eV}$  [52], respectively. Note that the pre-factor of  $1/2$  in *Eq. 2a* arises due to a mirror arrangement of two N(U)-vacancies on the surface and sub-surface layers.

The formation energies of N- and U-vacancies ( $E_{form}^{N(U) vac}$ ), calculated for the two reference states as functions of the slab thickness, are collected in Table 3. These are smallest for the surface layer and considerably increase (by  $\sim 0.6 \text{ eV}$  for the N-vacancy and by  $\sim 1.7 \text{ eV}$  for the U- vacancy) in the sub-surface and central layers, independently of the reference state. This indicates the trend for vacancy segregation at the interfaces (surfaces or crystalline grain boundaries). A weak dependence of  $E_{form}^{N(U) vac}$  on the slab thickness is also observed. The value of  $E_{form}^{N(U) vac}$  is saturated with the slab thicknesses of seven atomic layers and more. Moreover, the difference between values of  $E_{form}^{N(U) vac}$  for the 5- and 7- layer slabs is less for the surface

vacancies than for those in the central layer. This difference is the largest for the U-vacancy in the central plane ( $\sim 0.16$  eV).

The reference state II leads to smaller  $E_{form}^{N(U) vac}$  (as compared to those found for the reference state I) and demonstrates a significant difference for two types of vacancies. According to reference II, the U vacancy could be substantially easier formed at  $T = 0$  K than the N vacancy. Notice that the chemical potentials of O and U atoms used in similar defect studies in  $UO_2$  bulk did not reveal the energetic preference for the U-vacancy [50, 53]. The defect-defect interaction is not responsible for this effect as  $E_{form}^{N(U) vac}$  decreased by 0.1 eV only with the larger supercell size ( $3 \times 3$  in Table 3). On the other hand, the chemical potential of N may strongly depend on the temperature. For example, the formation energy of O-vacancy is reduced by almost 2 eV within a broad temperature range in perovskite oxides [54]. We, thus, expect that the trend will change of temperature effects are fully taken into account. Unlike the reference state II, the reference I results in similar formation energies for

Layer	Number of atomic planes and supercell extension (in brackets)	Reference I		Reference II	
		U	N	U	N
Surface layer	5 (2×2)	8.63	8.84	1.46	3.70
	7(2×2)	8.61	8.84	1.44	3.70
	9(2×2)	8.61	8.84	1.44	3.71
	11(2×2)	8.60	8.85	1.43	3.71
	5(3×3)	8.51	8.78	1.34	3.64
	7(3×3)	8.47	8.78	1.30	3.65
Sub- surface layer	5(2×2)	10.31	9.38	3.14	4.25
	7(2×2)	10.29	9.46	3.12	4.33
	9(2×2)	10.26	9.46	3.09	4.33
	11(2×2)	10.26	9.46	3.09	4.33
	7(3×3)	10.18	9.47	3.01	4.34
Central (mirror) layer <sup>c</sup>	5(2×2)	10.20	9.48	3.03	4.34
	7(2×2)	10.36	9.57	3.19	4.43
	9(2×2)	10.34	9.55	3.17	4.42
	11(2×2)	10.39	9.56	3.22	4.42
	7(3×3)	10.23	9.55	3.06	4.42

<sup>a</sup> reference energies I equal to -4.10 eV for U atom and -3.17 eV for N atom,

<sup>b</sup> reference energies II equal to -11.28 eV for U atom and -8.30 eV for N atom,

<sup>c</sup> defect formation energies for UN bulk using reference state I are 9.1-9.7 eV for the N- vacancy and 9.4-10.3 for the U-vacancy [38]

Table 3. The vacancy formation energies (in eV) for the two reference states (see the text for details).

both types of the vacancies. In the central slab layer, values of  $E_{form}^{N(U)vac}$  are similar to those in the bulk (Table 3).

## 5.2 Surface reconstruction induced by vacancies

The local atomic displacements around the vacancies are largest for the nearest neighbors of vacancies. The analysis of atomic displacements allows us to suggest that the U-vacancy disturbs the structure of the surface stronger than the N-vacancy. If the N-vacancy lies in the surface layer, displacements of the nearest U atoms in the  $z$ -direction achieve 0.02-0.05 Å towards the central plane of the slab. The displacements of N atom nearest to the surface N vacancy achieve 0.05 Å towards the central plane ( $z$ -direction) and 0.01 Å in the surface plane ( $xy$ -displacement). Maximum displacements of neighbor atoms around the N-vacancy in the central plane have been found to be 0.04-0.07 Å (nearest U atoms from the neighboring layers are shifted in the  $z$ -direction towards the vacancy) not exceeding 0.025 Å for all the other atoms in the slab.

In contrast, the formation of U-vacancy results in much larger displacements of neighboring atoms, irrespectively of its position. If this vacancy lies in the surface layer, the displacements of 0.3-0.32 Å for the nearest N atoms are observed. If the U-vacancy lies in the central layer, the nearest N atoms from this layer are displaced by 0.17 Å while the N-atoms from the nearest layers are not shifted in  $xy$ -direction, being shifted by 0.15 Å towards the slab surface in the  $z$ -direction. The atomic displacements around the vacancies in the bulk have been found to be -0.03 Å and 0.13 Å for the N- and U-vacancies, respectively [38]. These values are close to those found in the calculations discussed here for the vacancies in the central slab layer, which mimics the bulk properties.

## 5.3 Electronic properties and finite-size effects

The finite slab-size effects caused by relatively large concentration of defects could be illustrated using the difference electron density redistribution  $\Delta\rho(\mathbf{r})$ . In Fig. 4, these redistributions are shown for N-vacancies positioned at both the outer (surface) and the central (mirror) planes of 5- and 7-layer slabs. Presence of two symmetrically positioned vacancies in the 5-layer slab induces their weak interaction across the slab (Fig. 4a) illustrated by appearance of an additional electron density around the N atoms in the central plane of the slab. Similarly, the vacancy in the mirror plane disturbs the atoms in the surface plane if thin slab contains only 5 layers (Fig. 4c). By increasing the slab thickness, we can avoid the effect of finite-slab size (Figs. 4b,d) which explains the stabilization of formation energies calculated for the 7-layer and thicker UN(001) slabs (Table 3).

The densities of states (DOS) are presented in Fig. 5. for both perfect and defective 7-layer UN slab. The U(5f) electrons are localized close to the Fermi level. These electrons are still strongly hybridized with the N(2p) electrons. It confirms the existence of covalent bonding observed in the analysis of Bader charges for defect-free surface. The N(2p) states form a band of the width ~4 eV, similar to that obtained in the bulk [5, 38]. In contrast, the contribution of U(6d) electrons remains insensitive to the presence of vacancies since the corresponding levels are almost homogeneously distributed over a wide energy range including the conduction band.

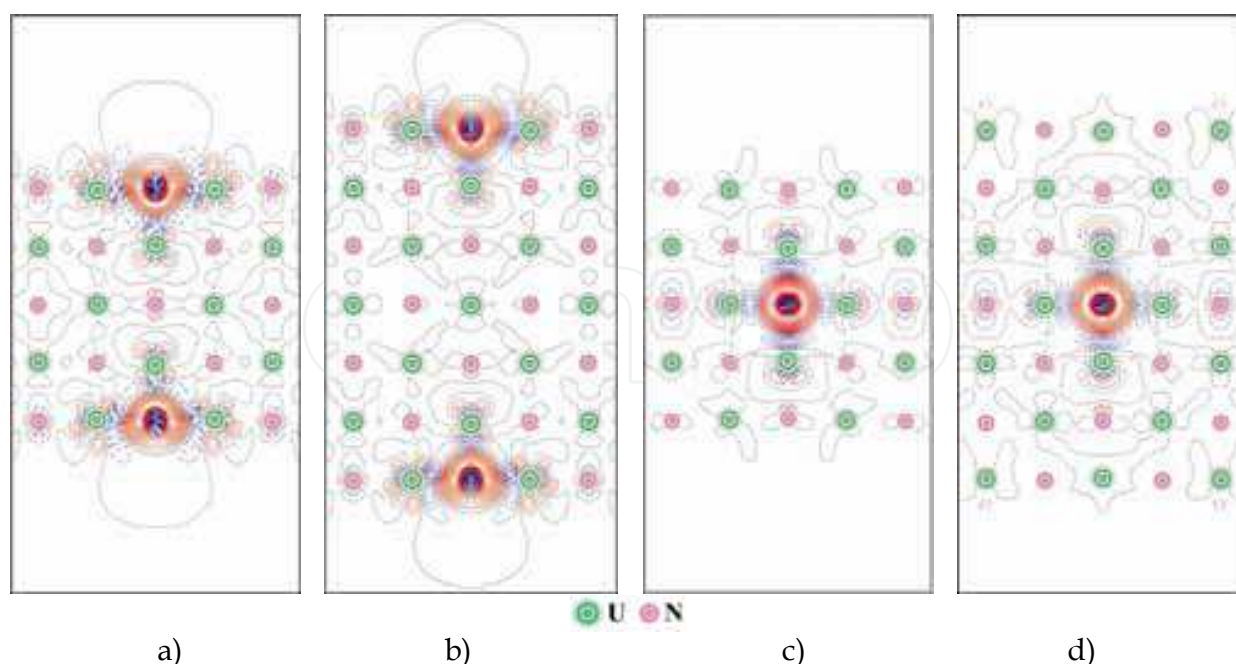


Fig. 4. The 2D sections of the electron density redistributions around the N-vacancies in the 5- and 7-layer (001) slabs (2×2) defined as the total electron density of defective surface minus a superposition of the electron densities for both perfect surface and isolated atom in the regular position on the surface: a) the N-vacancy in the surface plane, the 5-layer slab, b) the same for the 7-layer slab, c) the N-vacancy in the central plane, the five-layer slab, d) the same for the 7-layer slab. Solid (red) and dashed (blue) isolines correspond to positive (excess) and negative (deficiency) electron density, respectively. Isodensity increment is  $0.0025 e\cdot a.u.^{-3}$ .

#### 5.4 Comparison of the UN (001) and (110) surfaces

To increase the reliability of the results we compare also the results of point defect calculations in the surface layer of the (001) and the (110) surfaces (Table 4). Let us consider the 5-, 7-, 9-, and 11-layer 2×2 surface supercells as well as 7-layer 3×3 supercell for the (110) surface. The N-vacancy formation energies are by  $\sim 0.7$  eV smaller for the (110) surface. One can explain it due to a larger friability of the (110) surface as compared to the (001) surface. The dependence on the slab thickness is more pronounced for the (001) surface: the formation energy of N-vacancy increases with the thickness by 0.012 eV.

Number of layers and supercell size	(001)	(110)
5, 2×2	3.700	3.075
7, 2×2	3.706	3.028
9, 2×2	3.708	3.036
11, 2×2	3.712	3.026
7, 3×3	3.646	2.966

Table 4. The N-vacancy formation energies (in eV) evaluated for the (001) and (110) surfaces.

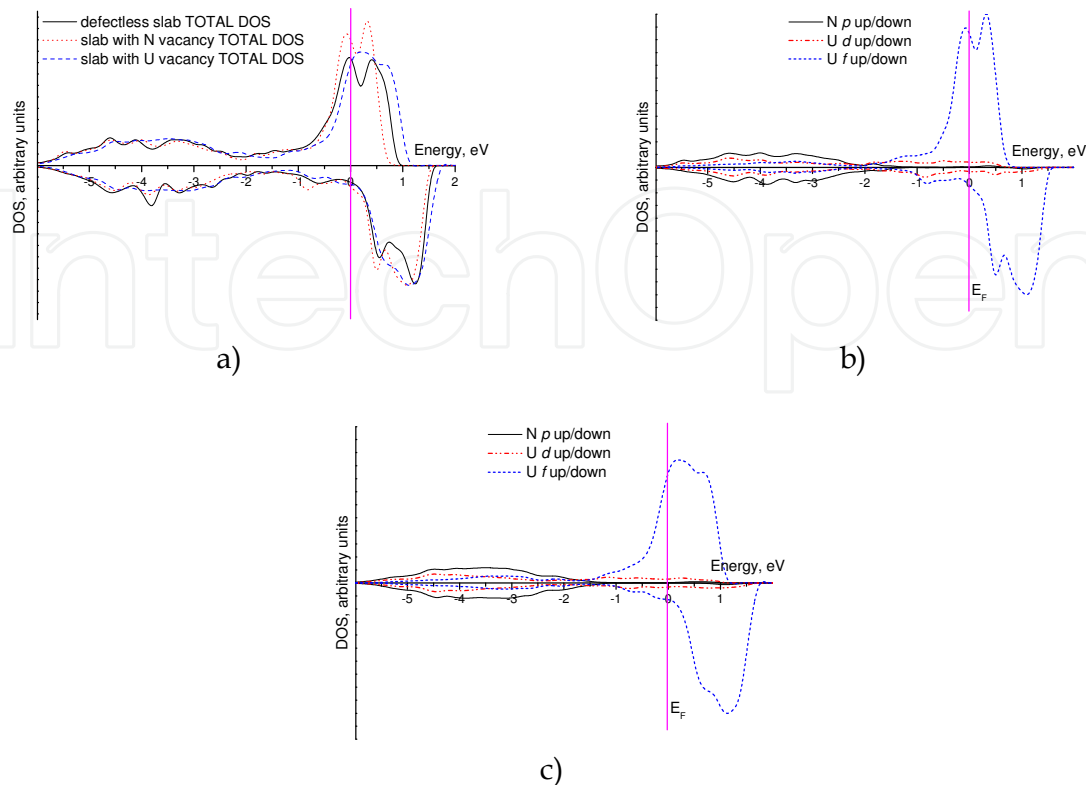


Fig. 5. The total and projected DOSs of the 7-layer (001) surface (2×2):  
 a) total DOS of defective and defect-free surfaces  
 b) projected DOSs for the surface containing the N-vacancies  
 c) projected DOSs for the surface containing the U-vacancies.

## 6. Molecular oxygen adsorption

### 6.1 Model and binding energy

The interaction of *molecular* oxygen  $O_2$  with the perfect UN(001) surface [7] and its dissociation on metallic UN surface will be considered here. It is important to consider prior simulations of O atom adsorption. An important issue for these interactions would be whether the  $O_2$  dissociation upon the surface is energetically possible, which adsorption sites are optimal for this, and whether it can occur spontaneously, without energy barrier, similarly to other metallic surfaces, for example Al [55].

Results as discussed here for molecular adsorption were performed using the fixed spin magnetic moment of U at  $1 \mu_B$ . We rely on this approximation, which allowed us to speed the calculations substantially up. In these simulations the 5-layer slab with the 2×2 supercell was used only. The periodic adsorbate distribution corresponds to the molecular coverage of 0.25 ML (or atomic O coverage of 0.5 ML). The binding energy  $E_{bind}$  per oxygen atom in the adsorbed molecule  $O_2$  was calculated as:

$$E_{bind} = \frac{1}{4} (E^{UN} + 2E^{O_2} - E^{O_2/UN}), \quad (4)$$

where  $E^{\text{O}_2/\text{UN}}$  the total energy of a fully relaxed  $\text{O}_2/\text{UN}(001)$  slab for several configurations of ( $\text{O}_2$ ) upon the surface (Fig. 6),  $E^{\text{O}_2}$  and  $E^{\text{UN}}$  the total energies of an isolated oxygen molecule in the ground (triplet) state and of a relaxed defectless UN slab, respectively. The pre-factor  $1/4$  appears due to the symmetrical slabs containing two equivalent surfaces with adsorbed  $\text{O}_2$ . Note that each molecule before and after dissociation contains two O atoms. When modeling the molecular adsorption, different configurations of the  $\text{O}_2$  molecule in the triplet state on surface are possible. *Vertical* orientations of the molecule were found to be unstable. But, the *horizontal* configurations suggest stable configurations. The binding energy of the molecule, using Eq. (4), and its dissociation energy (representing the difference of the total energies of a slab with an  $\text{O}_2$  molecule before and after dissociation) are given in Table 5.

## 6.2 Spontaneous dissociation

A spontaneous barrierless  $\text{O}_2$  dissociation indeed takes place in the two following cases, when the molecular center is atop either (i) a hollow site or (ii) N atom, with the molecular bond directed towards the two nearest U atoms (the configurations 1 and 5 in Fig. 6, respectively). The relevant dissociation energies  $E_{\text{diss}}$  are given in Table 5 together with other parameters characterizing the atomic relaxation and the Bader charge distribution. Geometry and charges for these configurations after dissociation are close to those obtained for chemisorbed O atoms (see the next section, too), i.e., the surface U atoms beneath the oxygen adatom after dissociation are shifted up in both configurations (Table 5). However, since concentration of O is twice as larger as compared to that for the atomic adsorption [6,10], some differences of the results still occur. These may be characterized by the *repulsion* energy of  $\sim 0.7$  eV between the two adatoms after  $\text{O}_2$  dissociation, which are positioned atop the two nearest U atoms (the configuration 1). Two more configurations of adsorbed  $\text{O}_2$  are possible, i.e. the dissociation is energetically possible with energy barrier: (i) atop the hollow site when a molecular bond is oriented towards the nearest N atoms (the configuration 2 in Fig. 6) and (ii) atop the U atom (for any molecular orientation, e.g., the configurations 3 and

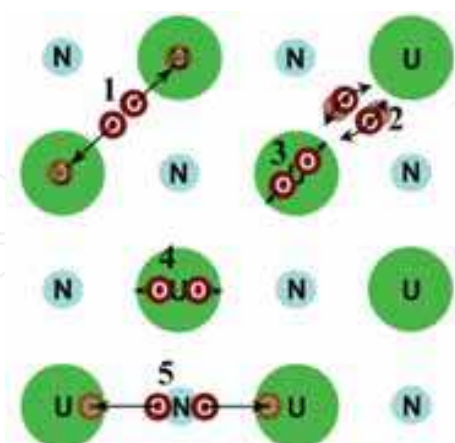


Fig. 6. Schematic view of five different horizontal configurations for the  $\text{O}_2$  molecule adsorption on UN (001) surface: 1) atop the hollow site between U atoms 2) atop the hollow site between N atoms 3) atop U atoms oriented towards the next-nearest surface U atoms 4) atop the U atoms oriented towards the nearest N atoms 5) atop the N atoms oriented towards the nearest U atoms. We show that spontaneous dissociation of molecule can occur when  $\text{O}_2$  is located either atop the hollow site (1) or atop the N atom (5).

4 in Fig. 6). For the configuration 2, the molecule rotates to take a stable position between the U atoms with further dissociation. The configurations 3 and 4 rather describe metastable  $\text{UO}_2$  quasi-molecules, due to a strong bonding between all three atoms, and, also because the corresponding U atom is noticeably shifted up from its initial positions on the surface. The dissociation of the  $\text{O}_2$  molecule in configuration 3 is energetically possible but only after overcoming the activation energy barrier.

Configuration		$E_{bind}$	$z^a$	$E_{diss}$	$\Delta z^e(\text{U1})$	$\Delta z^e(\text{U2})$	$\Delta z^e(\text{N})$
(1)	before dissociation	3.03	1.893	-	-0.050	-0.050	0.025
	after dissociation	6.04	1.957	3.01	0.075	0.068	-0.133
atop U	(3)	4.00	2.18	-	0.176	-0.048	-0.096
	(4)	4.18	2.14	-	0.123	-0.051	-0.106
(5)	before dissociation	2.67	2.020	-	-0.050	-0.050	0.025
	after dissociation	5.85	1.955	3.18	0.073	0.021	-0.201

<sup>a</sup>  $z$  is the height of O atoms with respect to the non-relaxed UN surface

<sup>e</sup>  $\Delta z$  the additional vertical shifts of the same surface atoms from their positions in absence of adsorbed oxygen.

Table 5. The calculated values of binding ( $E_{bind}$  per O atom in eV) and dissociation ( $E_{diss}$  in eV) energies as well as geometry ( $z$ ,  $\Delta z$  in Å) for molecular configurations and those for spontaneous dissociative chemisorption of  $\text{O}_2$ . The configurations are shown in Fig. 6. The calculated binding energy for a free  $\text{O}_2$  molecule in the triplet state is 6.06 eV and a bond length is 1.31 Å (cf. with experimental values of 5.12 eV and 1.21 Å, respectively) [56].

## 7. Modeling of O atom adsorption and migration on perfect UN surface

### 7.1 Model and binding energies

To simulate the O atom adsorption, we consider the 5- and 7-layer slabs for the (001) surface with the  $2 \times 2$  and  $3 \times 3$  supercell sizes (Figs 7-8). The binding energy  $E_{bind}$  of adsorbed oxygen atom is calculated with respect to a free O atom:

$$E_{bind} = \frac{1}{2} (E^{\text{UN}} + 2E^{\text{O}_{\text{triplet}}} - E^{\text{O/UN}}), \quad (5)$$

where  $E^{\text{O/UN}}$  the total energy of relaxed O/UN(001) slab for  $\text{O}_{\text{ads}}$  positions atop either the N or U surface ions,  $E^{\text{O}_{\text{triplet}}}$  and  $E^{\text{UN}}$  the energies of an isolated O atom in the ground (triplet) state and of a relaxed defectless UN slab. The free O atom is calculated in the cubic box with the edge of  $\sim 20$  Å. The pre-factor  $\frac{1}{2}$  appears since the surface is modeled by a slab with two equivalent surfaces and O is positioned symmetrically with respect to the central layer in the slab. We also can estimate  $E_{bind}$  in the case of the defective surface with one N vacancy in the surface layer according to

$$E_{bind} = \frac{1}{2} \left( E^{UN(N_{vac})} + 2E^{O_{triplet}} - E^{O/UN(N_{vac})} \right), \quad (6)$$

where  $E^{UN(N_{vac})}$  the total energy of defective UN substrate containing the N vacancy while  $E^{O/UN(N_{vac})}$  the total energy of adsorbed oxygen atoms atop the defective substrate (Table 6).

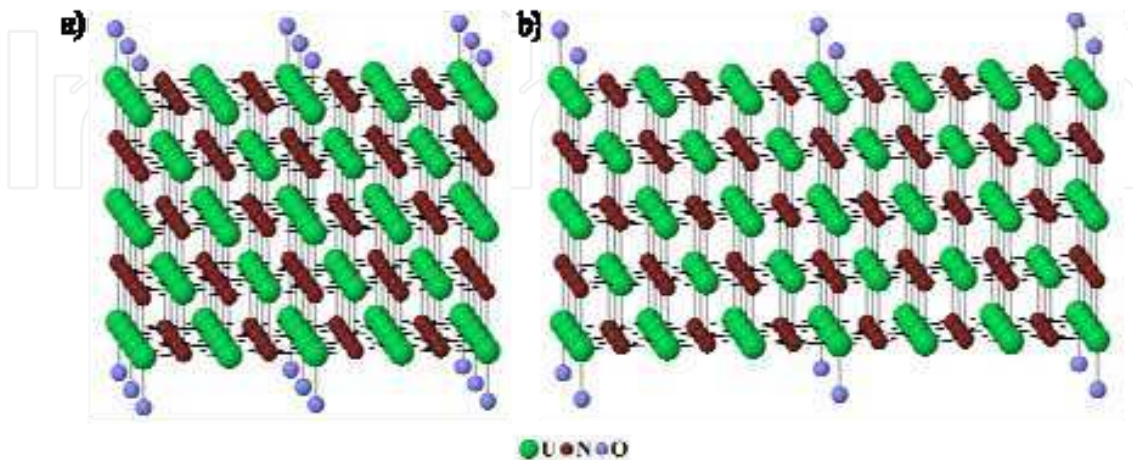


Fig. 7. Model of O/UN(001) interface: two-sided adsorption of O atoms regularly distributed atop  $U_{surf}$  atoms with the 2×2 (a) and 3×3 (b) periodicity

Due to a mixed metallic-covalent nature of the chemical bonding in UN, we expect a high affinity of adsorbed O towards the UN(001) surface. The binding energy *per* O adatom is expected to be similar to that on regular O/Al(111) and/or O/Al(001) metallic interfaces (~10 eV) [55] unlike that on semiconducting O/SrTiO<sub>3</sub>(001) interfaces (~2 eV) [57]. Indeed, the  $E_{bind}$  values of 6.9-7.6 and 5.0-5.7 eV *per* O adatom atop the surface U or N atoms, respectively, are accompanied by 0.5-1.2 *e* charge transfer from the surface towards the O adatom (Tables 6 and 7). The positively charged surface U atom goes outwards, minimizing its distance with the adsorbed O atom (Fig. 9). The N atom is strongly displaced from the adsorbed O atom inwards the slab, due to a mutual repulsion between N and O. Tables 6 and 7 clearly demonstrate the ionic character of surface O–U bond.

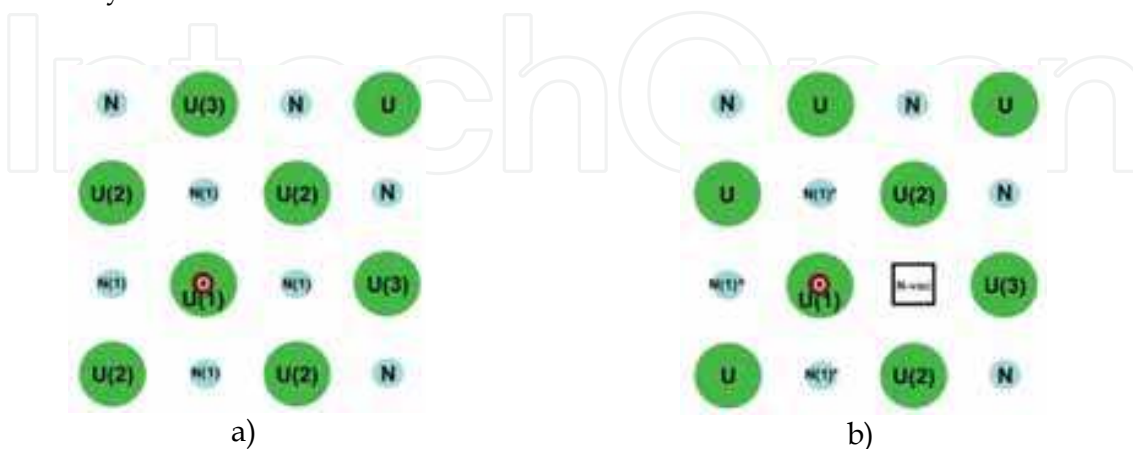


Fig. 8. Schematic top view of O adatoms located atop the surface U atom without (a) and with (b) N vacancy in the proximity of adsorbed O. Numbers in brackets enumerate non-equivalent surface atoms described in Tables 6 and 7.

Electron density redistributions caused by the absorption of O atom atop N or U atoms of the (001) surface are shown in Fig. 9. An analysis of the difference density plots for both configurations of O confirms that the oxygen adatom forms a strong bonding with the U atom which can be considered as one-center adsorption complex (Fig. 9c, 9d). In the case of O adatom atop the N atom, O atoms forms a multi-center adsorption complex involving four adjacent surface U atoms (Fig. 9a, 9b). As follows from Table 7, these surface atoms mostly contribute to the high O binding energy atop N. Formation of the strong chemical bonding of O atom with U results in a strong anisotropic redistribution of the electronic charges, thus, indicating considerable contribution of U 5*f*- and 6*d*-electrons to chemical bonding.

Model	$E_{bind}$	$q_O$	$q_{U(1)}$	$q_{U(2)}$	$q_{U(3)}$	$q_{N(1)}$	$d_{O-U}$	$\Delta z_{U(1)}$	$\Delta z_{U(2)}$	$\Delta z_{U(3)}$	$\Delta z_{N(1)}$
2x2 5-layers	7.57	-1.08	2.09	1.82	1.84	-1.63	1.88	+0.16	+0.025	+0.003	-0.09
2x2 7-layers	7.51	-1.08	2.19	1.78	1.78	-1.64	1.89	+0.17	+0.03	-0.02	-0.09
2x2 7-layers & N-vacancy	7.58 <sup>b</sup>	-1.08	1.84	1.50	1.48	-1.61 <sup>*</sup> -1.61 <sup>^</sup>	1.88	+0.14	+0.01	-0.02	-0.09 <sup>*</sup> -0.08 <sup>^</sup>
3x3 5-layers	7.59	-1.09	2.13	1.80	1.74	-1.62	1.88	+0.16	+0.01	-0.01	-0.10
3x3 7-layers	7.57	-1.09	2.13	1.78	1.79	-1.62	1.88	+0.16	+0.01	-0.01	-0.09
3x3 7-layers & N-vacancy	7.59 <sup>b</sup>	-1.09	1.86	1.47 <sup>*</sup>	1.38 <sup>*</sup>	-1.61 <sup>*</sup> -1.61 <sup>^</sup>	1.88	+0.10	-0.025 <sup>*</sup>	-0.06 <sup>*</sup>	-0.12 <sup>*</sup> -0.11 <sup>^</sup>

<sup>a</sup> positive sign corresponds to atom displacement outward the substrate; <sup>\*</sup> <sup>^</sup> adsorbed O atom in the presence of non-equivalent N atoms for system with the N-vacancy

Table 6. The binding energy ( $E_{bind}$  in eV), the equilibrium distance between O and surface U atom ( $d_{O-U}$  in Å), the effective atomic charges of atoms ( $q$  in  $e$ ), and vertical U and N atoms displacements ( $\Delta z$ )<sup>a</sup> from the surface plane for adatom position atop U. Values of  $q$  for the surface atoms on the perfect surface equal +1.68 (+1.74)  $e$  for U and -1.65 (-1.67)  $e$  for N [8].

Model	$E_{bind}$	$q_O$	$q_{N(1)}$	$q_{N(2)}$	$q_{N(3)}$	$q_{U(1)}$	$d_{O-N}$	$\Delta z_{N(1)}$	$\Delta z_{N(2)}$	$\Delta z_{N(3)}$	$\Delta z_{U(1)}$
2x2 5-layers	5.52	-1.17	-1.48	-1.68	-1.68	1.86	2.19	-0.69	+0.03	+0.05	+0.13
2x2 7-layers	5.58	-1.17	-1.48	-1.63	-1.67	1.86	2.21	-0.715	+0.03	+0.03	+0.12
3x3 5-layers	5.57	-1.18	-1.51	-1.67	-1.68	1.89	2.20	-0.70	+0.01	+0.01	+0.13
3x3 7-layers	5.65	-1.18	-1.51	-1.69	-1.65	1.89	2.22	-0.73	+0.01	+0.02	+0.12

<sup>a</sup> atomic positions of U and N ions are reversed as compared to those shown in Fig. 8a.

Table 7. The calculated parameters for O atom adsorbed atop N<sup>a</sup> (see caption and footnotes of Table 6 for explanation).

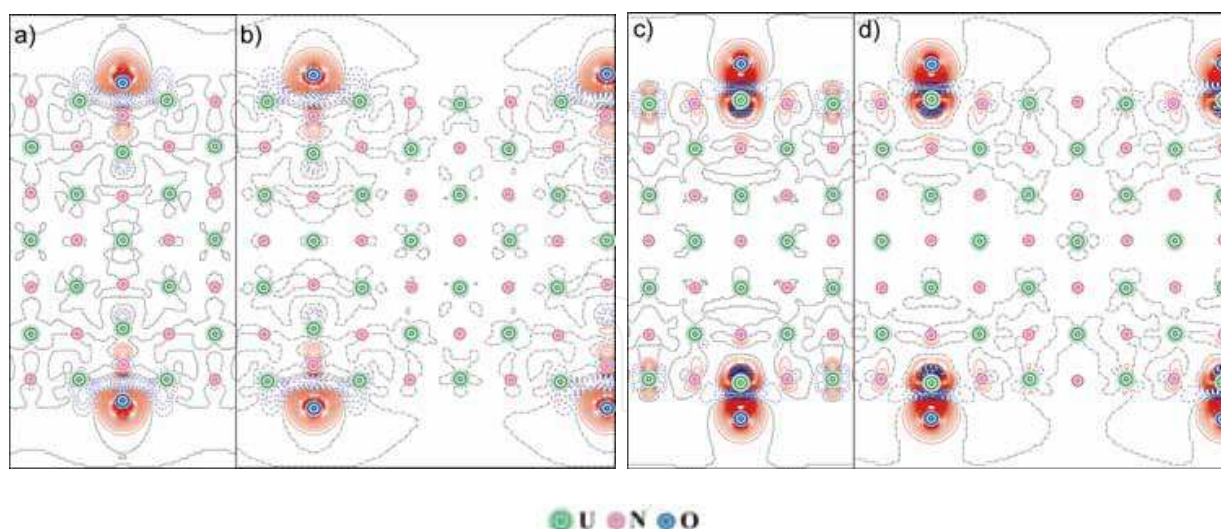


Fig. 9. The 2D sections of the electron charge density re-distributions  $\Delta\rho(\mathbf{r})$  for O atoms adsorbed atop (i) N atom for 2×2 (a) and 3×3 (b) supercells as well as (ii) U atom for 2×2 (c) and 3×3 (d) supercells upon the seven-layer UN(001) slab. Function  $\Delta\rho(\mathbf{r})$  is defined as the total electron density of the interface containing adsorbed O atom minus the densities of substrate and adsorbate with optimized interfacial geometry. Solid (red) and dashed (blue) isolines correspond to positive and negative electron densities, respectively. Dot-dashed black isolines correspond to the zero-level.

Plots of electronic density redistributions clearly show that the U atoms shield influence of neighbor atoms on the next coordination spheres much better than the N atoms.

From the viewpoint of finite size effects, the 3×3 supercell allows one to reduce the interactions between the adsorbed O atoms (as well vacancies if present). As seen in Table 7, the charges are slightly larger and displacements are smaller for larger supercells. The choice of supercell size influences the interactions between the defects across the slab. In particular, adsorption atop the N atom is sensitive to this effect.

## 7.2 Comparison of the UN (001) and (110) surfaces

The binding energies of oxygen adatom with UN(110) surface are given in Table 8. For both the surfaces, the binding energies with the U atom are larger as compared with the N atom (~1.9 eV for the (001) vs. ~2.1-2.2 eV for the (110) surface). Moreover, if the supercell size is

Number of layers and supercell size		U	N
(001)	7, 2×2	7.51	5.58
	7, 3×3	7.57	5.65
(110)	7, 2×2	7.90	5.73
	7, 3×3	7.91	5.99

Table 8. The calculated binding energies ( $E_{bind}$ , eV) for oxygen atom adsorption atop UN (001) and (110) surfaces.

increased from 2×2 to 3×3, then  $E_{bind}$  is also increased. The  $E_{bind}$  values on the (110) surface are ~0.1-0.4 eV larger as compared to the (001) one. Such higher  $E_{bind}$  values for the (110) surface could be explained by larger distances between the surface adatoms upon the (110) surface resulting in decreased lateral interactions between the adsorbed O atoms.

### 7.3 Migration path for O ad-atom

Three main migration paths of O upon the UN (001) surface (Fig. 10) are as follows [10]: (i) path 1: between U atom and the nearest N atom, (ii) path 2: between the two neighboring U atoms, (iii) path 3: between neighboring N atoms.

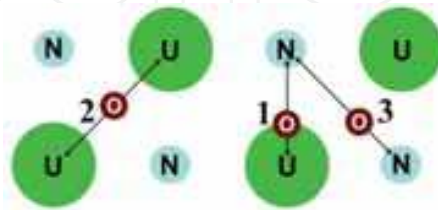


Fig. 10. Different oxygen migration paths upon the UN(001) surface (top view).

1. From site atop $U_{surf}$ to site atop N (migration path 1)				
<i>Supercell size:</i>	2×2		3×3	
<i>Number of atomic layers:</i>	5	7	5	7
atop U	7.57	7.51	7.59	7.57
1/4 of distance U-N (or 0.61 Å from U atom)	7.39	7.39	-	-
1/2 of distance U-N (or 1.22 Å from U atom)	6.97	6.98	-	-
3/4 of distance U-N (or 1.83 Å from U atom)	5.91	5.93	-	-
atop $N_{surf}$ (or 2.43 Å from U atom)	5.52 <sup>b</sup>	5.58	5.57	5.65
2. From hollow position (h.p.) to site atop U (migration path 2)				
<i>Supercell size:</i>	2×2		3×3	
<i>Number of atomic layers:</i>	5	7	5	7
atop h.p.	7.21	7.245	7.20	7.21
1/4 of distance h.p.-U (or 0.43 Å from h.p.)	7.23	7.255	-	-
1/2 of distance h.p.-U (or 0.86 Å from h.p.)	7.32	7.33	-	-
3/4 of distance h.p.-U (or 1.29 Å from h.p.)	7.45	7.45	-	-
atop $U_{surf}$ (or 1.72 Å from h.p.)	7.57	7.51	7.59	7.57
3. From hollow position (h.p.) to site atop $N_{surf}$ (migration path 3)				
<i>Supercell size:</i>	2×2		3×3	
<i>Number of atomic layers:</i>	5	7	5	7
atop h.p.	7.21	7.25	7.20	7.21
1/4 of distance h.p.-N (or 0.43 Å from h.p.)	6.61	6.65	-	-
1/2 of distance h.p.-N (or 0.86 Å from h.p.)	6.32	6.35	-	-
3/4 of distance h.p.-N (or 1.29 Å from h.p.)	5.54	5.57	-	-
atop $N_{surf}$ (or 1.72 Å from h.p.)	5.52	5.58	5.57	5.65

Table 9. Binding energies  $E_{bind}$  of O atoms in different positions atop UN slab (Fig. 10).

In contrast to adsorption calculations, only  $z$  coordinates of all atoms in the slab were relaxed in these migration calculations. The results of O migration for different slab thicknesses and supercell extensions are summarized in Table 9. These represent the values of binding energies calculated for migration paths of O adatoms upon the perfect UN(001) substrate shown in Fig. 10. We fix five sites along the O migration trajectories for  $2 \times 2$  supercells of UN(001) slab and two sites for  $3 \times 3$  supercells. In both cases, the most favorable migration trajectory has been optimized to be the line joining the sites atop the nearest surface U atoms and the hollow sites between them (trajectory 2). The corresponding energy barriers found (0.36 eV for the 5-layer slab and 0.26 eV for the 7-layer slab) indicate a high mobility of adsorbed O atoms upon UN. The energy barriers along other two migration trajectories are substantially larger (1.93-2.05 eV and 1.31-1.69 eV for trajectories 1 and 3 shown in Fig. 10). Thus, we predict quite high mobility of atoms along the surface, due to relatively low migration barriers.

## 8. Oxygen migration and incorporation into the surface vacancies

### 8.1 Model of ad-atom migration

To estimate the oxygen adatom mobility upon the defective UN(001) surface, we also have performed a series of calculations of O atom adsorbed atop the surface U atom in the proximity of the surface N-vacancy (Fig. 8b). According to our calculations, this O atom can be captured by the vacancy when overcoming a low energy barrier ( $\sim 0.5$ -1 eV). We have estimated the energy gain for such a transition of oxygen adatom using the formula:

$$\Delta E_g = \frac{1}{2} \left( E_{tot}^{UN(O\_in\_N\_vac)} - E_{tot}^{UN(O\_atop\_U)} \right), \quad (7)$$

where  $E_{tot}^{UN(O\_in\_N\_vac)}$  is the total energy of the supercell containing the O atom in the N-vacancy, and  $E_{tot}^{UN(O\_atop\_U)}$  the total energy of the supercell with O atom adsorbed atop U atom positioned in the proximity of existing N-vacancy. For calculations on the total energies in Eq. 7 we have fixed horizontal  $x$  and  $y$  oxygen coordinates, to prevent the O adatom migration. The pre-factor  $\frac{1}{2}$  in Eq. (7) appears due to the symmetric arrangement of adsorbed or incorporated O atoms. The calculated energy gain ( $\Delta E_g$ ) for the transition from position atop U atom to position in the N-vacancy equals to  $\sim 2$  eV *per* oxygen adatom (1.99 eV for  $2 \times 2$  7-layer supercell and 1.94 eV for  $3 \times 3$  7-layer supersell). Thus, we have showed the possibility of low-barrier oxygen adatom incorporation into existing the N-vacancy from the nearest adsorption site atop the U atom.

### 8.2 Oxygen incorporation and solution energies

The incorporation of O atom into the surface vacancies is expected along with oxygen atom diffusion along the surface or right after O<sub>2</sub> dissociation. One of possible ways for UN surface oxidation is the formation of oxynitride islands or films upon the UN surface [22]. The energies (of incorporation  $E_i$  and of solution  $E_s$  into the (001) surface) which characterize this process are discussed here. Hence, it is very important to describe the oxygen interaction with the single vacancies. As known from the literature, considerable attention was paid so far to the static and dynamic properties of primary defects

(vacancies and incorporated impurities) in UN *bulk* [38]. These defects affect the fuel performance during operation and its reprocessing. Apart from the behavior of empty vacancies, the O atom incorporation into them in bulk UN was also considered. Incorporation of O into the N-vacancy in the bulk was found to be energetically more favorable in comparison with the interstitial sites [58]. However,  $E_S$  demonstrates an opposite behavior.

Our calculations have been performed for surface 2×2 and 3×3 UN supercells. The O atom can occupy either the N- or U-vacancies in the surface, sub-surface and central layers of the slab. Due to the presence of mirror layers in the symmetric slabs, one can consider the two-sided symmetric arrangement of defects.

The energy balance for the incorporation of an O atom into a vacancy can be characterized by the incorporation energy  $E_I$  as suggested by Grimes and Catlow [59]

$$E_I = E^{\text{UN(O}_{-}\text{inc})} - E^{\text{UN(N/U}_{-}\text{vac})} - E^{\text{O}}, \quad (8a)$$

for the O atom incorporated into the N- and U vacancy in the central atomic layer and

$$E_I = \frac{1}{2}(E^{\text{UN(O}_{-}\text{inc})} - E^{\text{UN(N/U}_{-}\text{vac})} - 2E^{\text{O}}), \quad (8b)$$

for the same incorporation in the surface or sub-surface layers. Here  $E^{\text{UN(O}_{-}\text{inc})}$  the total energy of the supercell containing the O atom at either the N- or U-vacancy ( $E^{\text{UN(O}_{-}\text{inc})} < 0$ ),  $E^{\text{UN(N/U}_{-}\text{vac})}$  the energy of the supercell containing an unoccupied (empty) vacancy, and  $E^{\text{O}}$  half the total energy of isolated O<sub>2</sub> molecule in the triplet state (representing the oxygen chemical potential of O at 0 K). Since the value of  $E_I$  describes the energy balance for the incorporation into pre-existing vacancies, it has to be negative for energetically favorable incorporation processes.

To take into account the total energy balance, including the vacancy formation energy  $E_{form}$  in the defect-free slab, the solution energy [59] is defined as:

$$E_S = E_I + E_{form}, \quad (9)$$

where  $E_{form}$  the formation energy of N- or U-vacancy in the slab calculated using *Eqs. 2a* and *2b*. The parameters and properties of calculated O<sub>2</sub> molecule and  $\alpha$ -U are the same as discussed in previous sections.

The calculated O adatom incorporation into the N-vacancy of the UN(001) surface has been found to be energetically favorable since both values of  $E_I$  and  $E_S$  are strictly negative (Table 10). This is in favor of both creation of the N vacancy and adsorption of the O atom from air. Also,  $E_I$  decreases by ~0.4 eV (becomes more negative) within the slab as compared to the surface layer, whereas  $E_S$  is smallest for the N-vacancy just on the surface layer. Contrary, the values of  $E_I$  for the surface and central layers have been found to be close to zero in case of U-vacancy. The sub-surface layer is characterized by ~1 eV smaller values of  $E_I$  than for the surface and central layers. Our results indicate importance of oxynitride formation. However,  $E_S$  is positive and increases for O atoms in the U-vacancy and the slab center.

Table 10 also indicates that solution of oxygen atoms is energetically more favorable at the surface layers than inside the slab. As the supercell size increases (see the 3×3 extension in Table 10), both  $E_I$  and  $E_S$  decrease whereas influence of the slab thickness is not so clear. Nevertheless, the U-vacancy appeared to be most sensitive to the supercell size related to spurious interactions between the periodically repeated defects. The  $E_I$  as well as  $E_S$  values may be reduced by 0.15 eV at the average in this case.

Layer	Supercell size	Number of layers	N			U		
			$E_I$	$E_S$	$q_{eff}$	$E_I$	$E_S$	$q_{eff}$
Surface	2×2	5	-6.17	-2.47	-1.36	-0.34	1.12	-0.98
		7	-6.18	-2.48	-1.36	-0.86	0.58	-1.03
		9	-6.19	-2.48	-1.36	-0.94	0.49	-1.06
	3×3	5	-6.12	-2.48	-1.37	-0.68	0.654	-1.05
		7	-6.13	-2.48	-1.36	-1.07	0.230	-1.08
Subsurface	2×2	5	-6.31	-2.07	-1.42	-1.86	1.284	-1.10
		7	-6.42	-2.09	-1.40	-1.82	1.297	-1.10
		9	-6.42	-2.09	-1.40	-1.82	1.271	-1.10
	3×3	7	-6.43	-2.09	-1.39	-2.01	1.000	-1.10
Central (mirror)	2×2	7	-6.61	-2.18	-1.42	0.74	3.923	-0.89
		9	-6.61	-2.19	-1.38	0.67	3.838	-0.90
	3×3	7	-6.60	-2.18	-1.42	0.32	3.378	-0.94

Table 10. The incorporation ( $E_I$ ) and solution ( $E_S$ ) energies (in eV), effective charge of oxygen atoms ( $q$  in  $e^-$ ) for the O incorporation. The reference states for incorporation and solution energies into the U- and N-vacancies are the chemical potentials of O, N and U (see the text for details).

### 8.3 Electronic properties and finite-size effects

Large concentrations of defects (25% for the 2×2 extension in Table 10) causes certain finite-size effects which can be illustrated using the 2D difference electron density redistributions  $\Delta\rho(\mathbf{r})$ . These plots are shown for the O atoms incorporated into the N-vacancies at the surface (Fig. 11). Inside the 5-layer slab, a presence of the two symmetrically positioned defects induces their interaction (visible in charge redistribution across a slab in Fig. 11a). An increase of the slab thickness reduces this effect (Fig. 11c). If the supercell size is decreased (the 2×2 supercell, Fig. 11b) an additional electron density parallel to the surface layer is observed between the defects. The results of the analysis of supercell size effects are

similar to those for pure vacancies. However, in the case of surface U-vacancy and O atom, a larger concentration of electron density was observed between the O atom and neighbouring N atoms in the sub-surface layer in a comparison to the pure N-vacancy. Thus, the effect of slab thickness may not be ignored here, too.

In Fig. 12, the total and projected densities of states are shown for the 7-layer defective UN(001) surface with the O atom incorporated into the N-vacancy. The system remains conducting throughout all the calculations with the significant contribution from the U(5*f*) states at the Fermi level similar to perfect UN(001) slab. The appearance of specific O(2*p*) band with the energy peak at -6 eV is observed. a noticeable shift of the O(2*p*) band (by about -1.0 eV) allows one to distinguish the surface layer from the internal layers, when comparing the DOS for the O atoms incorporated into the N-vacancies.

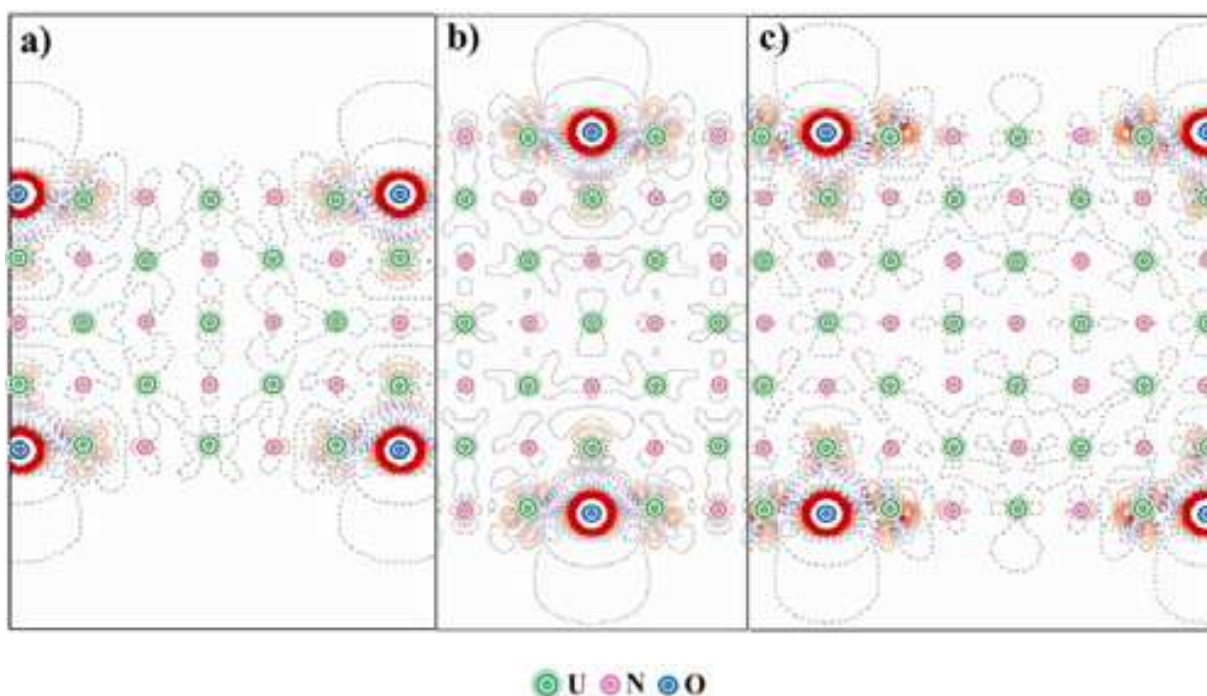


Fig. 11. The 2D sections of the electron charge density re-distributions  $\Delta\rho(\mathbf{r})$  around the O atoms incorporated into the surface N-vacancies of the 5- and 7-layer UN(001) slabs with  $2\times 2$  and  $3\times 3$  supercell extensions.  $\Delta\rho(\mathbf{r})$  are defined as the total electron density of the O-containing defected surface minus a superposition of the electron densities of the surface containing the N vacancies and the O atom in the regular positions on the surface. a)  $3\times 3$  periodicity of the O atoms upon the five-layer slab, b)  $2\times 2$  periodicity of the O atoms upon the seven-layer slab, c)  $3\times 3$  periodicity of the O atoms upon the 7-layer slab. Other details are given in caption of Fig. 9.

Moreover, in the case of surface layer, this band considerably overlaps with the N(2*p*) band, partly mixed with the U(5*f*) states (similar effects occur with the O<sub>2</sub> molecule atop the surface U atom [6]). In contrast, the O(2*p*) band remains quasi-isolated from the other bands (analogously to the O atom incorporated into the N-vacancy in the UN bulk [58]). Position of the N(2*p*) band is insensitive to presence of O atoms and lies within energy range of -6 and -1 eV.

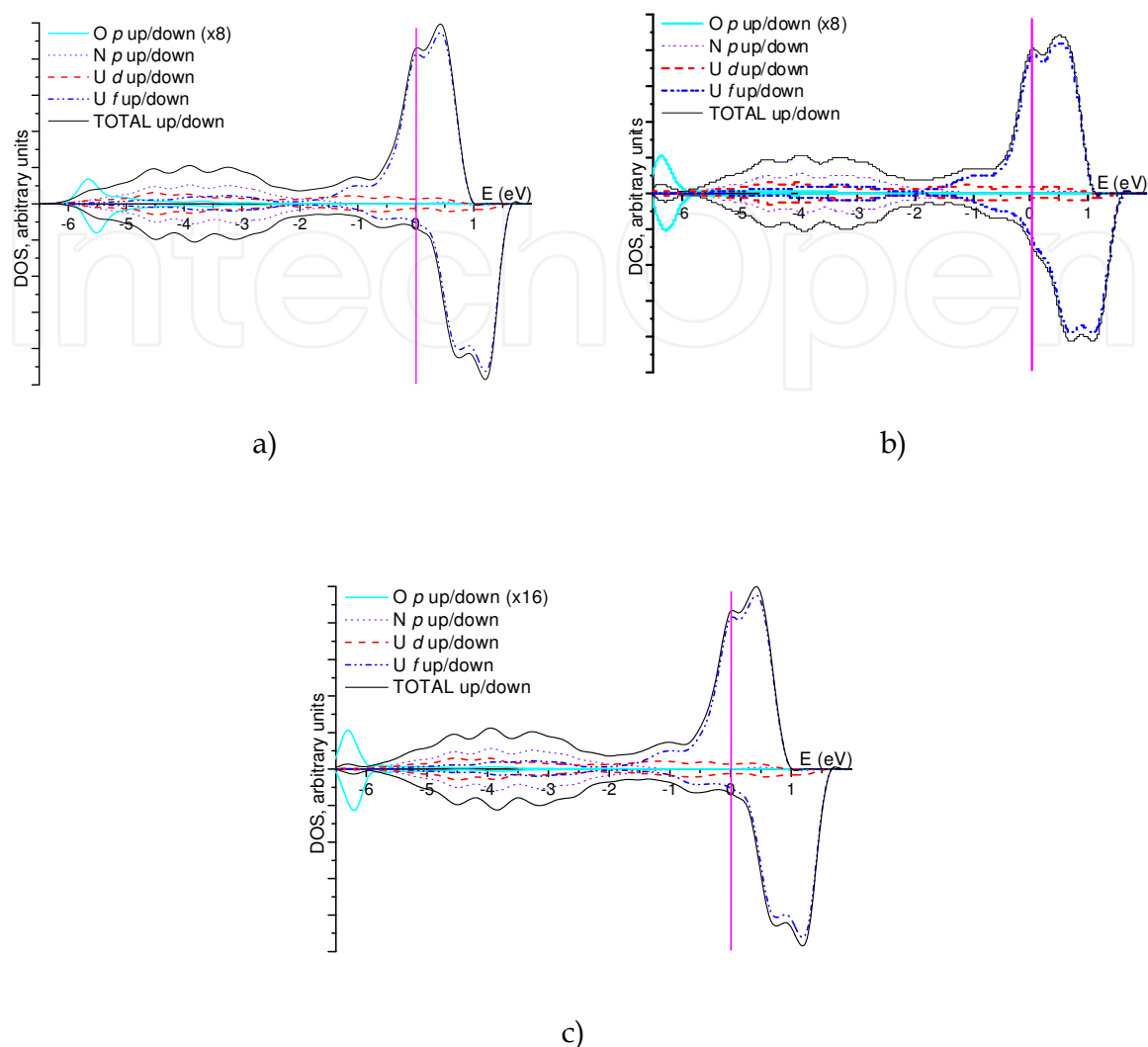


Fig. 12. The total and projected DOS for three positions of O atoms incorporated into the N-vacancies of the 7-layer UN(001) slab with the 3x3 supercell: a) surface layer b) sub-surface layer, c) central layer. The O(2p) peaks were normalized to the same value, i.e., these have been multiplied by a factor of 8 and 16 for the vacancies in the surface (sub-surface) and central layers, respectively (see Figure labels). A convolution of individual energy levels was plotted using the Gaussian functions with a half-width of 0.2 eV.

#### 8.4 Comparison of the UN (001) and (110) surfaces

Table 11 compares  $E_S$  and  $E_I$  for the two surfaces as functions of the slab thickness and supercell size. One can see that the UN(110) surface is characterized by more negative  $E_S$  even though the difference between the solution energies is  $\sim 0.3$  eV only. On the other hand,  $E_I$  is characterized by an opposite trend, suggesting more negative values for the (001) surface. Moreover, the difference between  $E_I$  for the two surfaces approaches 0.4 eV. Such results demonstrate importance of the  $E_I$  calculations, as the role of different surfaces may also change with the temperature. Nevertheless, we clearly see similar trends for both of the surfaces (Table 11).

Model	$E_I$	$E_S$	$q_{eff}$	$E_I$	$E_S$	$q_{eff}$
	(001) surface			(110) surface		
5, 2×2	-6.17	-2.47	-1.36	-5.85	-2.78	-1.27
7, 2×2	-6.18	-2.48	-1.36	-5.82	-2.79	-1.29
9, 2×2	-6.19	-2.48	-1.36	-5.82	-2.78	-1.29
11, 2×2	-6.20	-2.48	-1.35	-5.82	-2.79	-1.29
7, 3×3	-6.13	-2.48	-1.36	-5.75	-2.78	-1.28

Table 11. Incorporation ( $E_I$ ) and solution ( $E_S$ ) energies, effective charge of O atoms ( $q$  in  $e^-$ ) for O incorporated into the N-vacancy of the UN (001) and (110) surfaces. The reference states were the same as in Table 10.

## 9. Conclusions

Based on the results of calculations discussed above the following stages of oxygen interaction with the UN surfaces were indentified to explain its easy oxidation: (i) chemisorption of molecular oxygen, (ii) spontaneous breaking of the  $O_2$  chemical bond after molecular adsorption, (iii) location of the two newly formed O adatoms atop the adjacent surface U atoms, (iv) high mobility of adsorbed O atoms along the surface, (v) low-barrier incorporation of O into N-vacancies, (vi) stabilization of O atom inside the N-vacancy, (vii) further incorporation of O in pre-existed sub-surface N-vacancies as a result of inter-layer diffusion.

## 10. Acknowledgments

This study was partly supported by the EC FP7 F-BRIDGE project, ERAF project No. 2010/0204/2DP/2.1.1.2.0/10/APIA/VIAA/010, and ESF project No. 2009/0216/1DP/1.1.1.2.0/09/APIA/VIAA/044. Authors are indebted to P. van Uffelen, R.A. Evarestov, R. Devanathan, M. Freyss, E. Heifets, V. Kashcheyevs, Yu. A. Mastrikov, and S. Piskunov for helpful discussions. The technical assistance of A. Gopejenko, A. Gusev and A. Kuzmin was the most valuable.

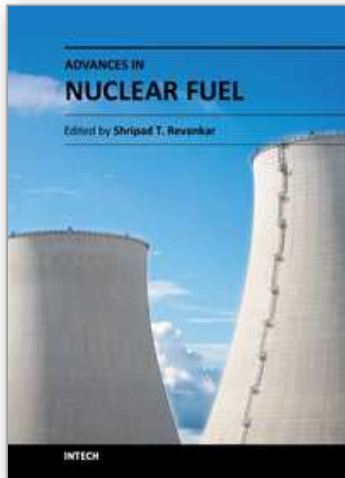
## 11. References

- [1] H.J. Matzke, Science of Advanced LMFBR Fuel, North Holland, Amsterdam, 1986.
- [2] The Nuclear Fuel Cycle. P.D. Wilson (Eds.), University Press, Oxford, 1996.
- [3] H. Wiame, M. Centeno, S. Pacard, P. Bastian, and P. Grange, Thermal oxidation under oxygen of zirconium nitride studied by XPS, DRIFTS, TG-MS. - J. Eur. Ceram. Soc., 1998, 18, p. 1293-1299.
- [4] M. Walter, Oxidation of inert matrices, JRC-ITU-TN-2005/35 (Research report).
- [5] R.A. Evarestov, A.V. Bandura, M.V. Losev, E.A. Kotomin, Yu.F. Zhukovskii, and D. Bocharov, A first principles DFT study in UN bulk and (001) surface: Comparative LCAO and PW calculations. - J. Comput. Chem., 2008, 29, p. 2079-2087.

- [6] Yu.F. Zhukovskii, D. Bocharov, E.A. Kotomin, R.A. Evarestov, and A.V. Bandura, First principles calculations of oxygen adsorption on the UN(001) surface. - Surf. Sci., 2009, 603, p. 50-53.
- [7] Yu.F. Zhukovskii, D. Bocharov, and E.A. Kotomin, Chemisorption of a molecular oxygen on the UN (001) surface: *ab initio* calculations. - J. Nucl. Mater., 2009, 393, p. 504-507.
- [8] D. Bocharov, D. Gryaznov, Yu.F. Zhukovskii, and E.A. Kotomin, DFT calculations of point defects on UN(001) surface. - Surf. Sci., 2011, 605, p. 396-400.
- [9] D. Bocharov, D. Gryaznov, Yu.F. Zhukovskii, E.A. Kotomin, *Ab initio* modeling of oxygen impurity atom incorporation into uranium mononitride surface and subsurface vacancies. - J. Nucl. Mater., 2011, 416, p.200-204.
- [10] D. Bocharov, Yu.F. Zhukovskii, D. Gryaznov, and E.A. Kotomin, *Ab initio* simulation on oxygen adatom migration upon UN (001) surface. - Surf. Sci., *submitted*.
- [11] N. Curry, An investigation of the magnetic structure of uranium nitride by neutron diffraction. - Proc. Phys. Soc., 1965, 86, p. 1193-1198.
- [12] T. Muromura and H. Tagawa, Lattice parameter of uranium mononitride. - J. Nucl. Mater., 1979, 79, p. 264-266.
- [13] P.E. Evans and T.J. Davies, Uranium nitrides. - J. Nucl. Mater., 1963, 10, p. 43-55.
- [14] N.-T.H. Kim-Ngan, A.G. Balogh, L. Havela, and T. Gouder, Ion beam mixing in uranium nitride thin films studied by Rutherford Backscattering Spectroscopy. - Nucl. Instr. Meth. Phys. Res. B, 2010, 268, p. 1875-1879.
- [15] P.R. Norton, R.L. Tapping, D.K. Creber, and W.J.L. Buyers, Nature of the 5*f* electrons in uranium nitride: A photoelectron spectroscopic study of UN, U, UO<sub>2</sub>, ThN, and Th. - Phys. Rev. B, 1980, 21, p. 2572-2577.
- [16] T. Ito, H. Kumigashira, S. Souma, T. Tahakashi, and T. Suzuki, High-resolution angle-resolved photoemission study of UN and USb; Dual character of 5*f* electrons. - J. Magn. Magn. Mater., 2001, 226-230, p. 68-69.
- [17] M. Marutzky, U. Barkow, J. Schoenes, and R. Troć, Optical and magneto-optical properties of single crystalline uranium nitride. - J. Magn. Magn. Mater., 2006, 299, p. 225-230.
- [18] M. Paljević and Z. Despotović, Oxidation of uranium mononitride. - J. Nucl. Mater., 1975, 57, p. 253-257.
- [19] Y. Arai, M. Morihira, and T. Ohmichi, The effect of oxygen impurity on the characteristics of uranium and uranium-plutonium mixed nitride fuels. - J. Nucl. Mater., 1993, 202, p. 70-78.
- [20] L. Black, F. Miserque, T. Gouder, L. Havela, J. Rebizant, and F. Wastin, Preparation and photoelectron spectroscopy study of UN<sub>x</sub> thin films. - J. Alloys Comp., 2001, 315, p. 36-41.
- [21] G.W. Chinthaka Silva, Ch.B. Yeaman, L. Ma, G.S. Cerefice, K.R. Czerwinski, and A.P. Sattelberger, Microscopic characterization of uranium nitrides synthesized by oxidative ammonolysis of uranium tetrafluoride. - Chem. Mat., 2008, 20, p. 3076-3084.
- [22] M. Eckle, and T. Gouder, Photoemission study of UN<sub>x</sub>O<sub>y</sub> and UC<sub>x</sub>O<sub>y</sub> in thin films. - J. Alloys Comp., 2004, 374, p. 261-264.
- [23] S. Sunder and N.H. Miller, XPS and XRD studies of corrosion of uranium nitride by water. - J. Alloys Comp., 1998, 271-273, p. 568-572.

- [24] B. Reihl, G. Hollinger, and F.J. Himpsel, Itinerant 5*f*-electron antiferromagnetism in uranium nitride: A temperature-dependent angle-resolved photoemission study. - *Phys. Rev. B*, 1983, 28, p. 1490-1494.
- [25] P. Weinberger, C.P. Mallett, R. Podloucky, and A. Neckel, The electronic structure of HfN, TaN and UN. - *J. Phys. C: Solid St. Phys.*, 13, 1980, p. 173-187.
- [26] M.S. Brooks and D. Glötzel, Some aspects of the electronic structure of uranium pnictides and chalcogenides. - *Physica B*, 1980, 102, p. 51-58.
- [27] M.S. Brooks, Electronic structure of NaCl-type compounds of the light actinides. I. UN, UC, and UO. - *J. Phys. F: Met. Phys.*, 1984, 14, 639-652.
- [28] D. Sedmidubsky, R.J.M. Konings, and P. Novak, Calculation of enthalpies of formation of actinide nitrides. - *J. Nucl. Mater.*, 2005, 344, p. 40-44.
- [29] G.K. Johnson and E.H.P. Cordfunke, The enthalpies of formation of uranium mononitride and  $\alpha$ - and  $\beta$ -uranium sesquinitride by fluorine bomb calorimetry. - *J. Chem. Thermodyn.*, 1981, 13, p. 273-282.
- [30] R. Atta-Fynn and A.K. Ray, Density functional study of the actinide nitrides. - *Phys. Rev. B*, 2007, 76, 115101 (p. 1-12).
- [31] P.F. Weck, E. Kim, N. Balakrishnan, F. Poineau, C.B. Yeaman, and K.R. Czerwinski, First-principles study of single-crystal uranium mono- and dinitride. - *Chem. Phys. Lett.*, 2007, 443, p. 82-86.
- [32] Y. Lu, B.-T. Wang, R.-W. Li, H. Shi, and P. Zhang, Structural, electronic, and thermodynamic properties of UN: Systematic density functional calculations. - *J. Nucl. Mater.*, 2010, 406, p. 218-222.
- [33] B. Dorado, B. Amadon, M. Freyss, and M. Bertolus, DFT+*U* calculations of the ground state and metastable states of uranium dioxide. - *Phys. Rev. B*, 2010, 79, 235125 (p. 1-8)
- [34] B. Dorado, G. Jomard, M. Freyss, and M. Bertolus, Stability of oxygen point defects in UO<sub>2</sub> by first-principles DFT+*U* calculations: Occupation matrix control and Jahn-Teller distortion. - *Phys. Rev. B*, 2010, 82, 035114 (p. 1-11).
- [35] D. Gryaznov, E. Heifets and E.A. Kotomin, *Ab initio* DFT+*U* study of He atom incorporation into UO<sub>2</sub> crystals. - *Phys. Chem. & Chem. Phys.*, 2009, 11, p. 7241-7247.
- [36] D. Rafaja, L. Havela, R. Kuel, F. Wastin, E. Colineau, and T. Gouder, Real structure and magnetic properties of UN thin films. - 2005, 386, p. 87-95.
- [37] E.A. Kotomin, Yu.A. Mastrikov, Yu.F. Zhukovskii, P. Van Uffelen, and V.V. Rondinella, First-principles modelling of defects in advanced nuclear fuels. - *Phys. Stat. Sol. (c)*, 2007, 4, p. 1193-1196.
- [38] E.A. Kotomin, R. W. Grimes, Yu. A. Mastrikov, and N.J. Ashley, Atomic scale DFT simulations of point defects in uranium nitride. - *J. Phys.: Cond. Mat*, 2007, 19, 106208 (p. 1-9).
- [39] D. Gryaznov, E. Heifets, D. Sedmidubsky, Density functional theory calculations on magnetic properties of actinide compounds, *Phys. Chem. & Chem. Phys.*, 2010, 12, p. 12273-12278.
- [40] E.A. Kotomin, D. Gryaznov, R.W. Grimes, D. Parfitt, Yu.F. Zhukovskii, Yu.A. Mastrikov, P. Van Uffelen, V.V. Rondinella, and R.J.M. Konings, First-principles modelling of radiation defects in advanced nuclear fuels. - *Nucl. Instr. Meth. Phys. Res. B*, 2008, 266, p. 2671-2675.

- [41] G. Kresse and J. Furthmüller, *VASP the Guide*, University of Vienna, 2009; <http://cms.mpi.univie.ac.at/vasp/>
- [42] J. Hafner, *Ab initio* simulations of materials using VASP: Density-Functional Theory and beyond. - *J. Comput. Chem.*, 2008, 29, p. 2044–2078.
- [43] G. Kresse and J. Furthmüller, Efficient iterative schemes for *ab initio* total-energy calculations using a plane-wave basis set. - *Phys. Rev. B*, 1996, 54, p. 11169–11186.
- [44] G. Kresse and D. Joubert, From ultrasoft pseudopotentials to the projector augmented-wave method. - *Phys. Rev. B*, 1999, 59, p. 1758–1775.
- [45] H.J. Monkhorst and J.D. Pack, Special points for Brillouin-zone integrations. - *Phys. Rev. B*, 1976, 13, p. 5188–5192.
- [46] P.W. Tasker, The stability of ionic crystal surfaces. - *J. Phys. C: Solid State Phys.*, 1979, 12, p. 4977–4984.
- [47] J. Akella, S. Weir, J. M. Wills, and P. Söderlind, Structural stability in uranium. - *J. Phys.: Condens. Matter*, 1997, 9, L549 (p. 1-7).
- [48] C.G. Van de Walle and J. Neugebauer, First-principles calculations for defects and impurities: Applications to III-nitrides. - *J. Appl. Phys.*, 2004, 95, p. 3851–3879.
- [49] P. Söderlind, First-principles elastic and structural properties of uranium metal. - *Phys. Rev. B*, 2002, 66, 085113 (p. 1-7).
- [50] B. Dorado, M. Freyss, and G. Martin, GGA+*U* study of the incorporation of iodine in uranium dioxide. - *Eur. Phys. J. B*, 2009, 69, p. 203–210.
- [51] M. Freyss, First-principles study of uranium carbide: Accommodation of point defects and of helium, xenon, and oxygen impurities. - *Phys. Rev. B*, 2010, 81, 014101 (p. 1-16).
- [52] D.R. Lide (ed.), *CRC Handbook of Chemistry and Physics*, 88<sup>th</sup> Edition, CRC Press (2007–2008).
- [53] M. Iwasawa, Y. Chen, Y. Kaneta, T. Ohnuma, H. Y. Geng, and M. Kinoshita, First-principles calculation of point defects in uranium dioxide. - *Mat. Trans*, 2006, 47, p. 2651–2657.
- [54] D. Gryaznov, M. Finnis, HPC-Europa2, Science and Supercomputing in Europe, Research Highlights, 2010, p. 127  
<http://www.hpc-europa.org/files/SSCinEurope/CD2010/contents/127-material-Denis.pdf>
- [55] Yu.F. Zhukovskii, P.W.M. Jacobs, and M. Causà, On the mechanism of the interaction between oxygen and close-packed single-crystal aluminum surfaces. - *J. Phys. Chem. Solids*, 2003, 64, p. 1317–1331.
- [56] R. Weast, *CRC Handbook of Chemistry and Physics*. CRC Press Inc., Boca Baton (FL), 1985.
- [57] S. Piskunov, Yu.F. Zhukovskii, E.A. Kotomin, E. Heifets, and D. E. Ellis, Adsorption of atomic and molecular oxygen on the SrTiO<sub>3</sub>(001) surfaces: Predictions by means of hybrid density functional calculations. - *MRS Proc.*, 2006, 894, LL08-05 (p. 1-6).
- [58] E. A. Kotomin and Yu.A. Mastrikov, First-principles modelling of oxygen impurities in UN nuclear fuels. - *J. Nucl. Mater.*, 2008, 377, p. 492–495.
- [59] R. W. Grimes and C.R.A. Catlow, The stability of fission products in uranium dioxide. - *Phil. Trans. Roy. Soc. A*, 1991, 335, p. 609–634.



### **Advances in Nuclear Fuel**

Edited by Dr. Shripad T. Revankar

ISBN 978-953-51-0042-3

Hard cover, 174 pages

**Publisher** InTech

**Published online** 22, February, 2012

**Published in print edition** February, 2012

Worldwide there are more than 430 nuclear power plants operating and more plants are being constructed or planned for construction. For nuclear power to be sustainable the nuclear fuel must be sustainable and there should be adequate nuclear fuel waste management program. Continuous technological advances will lead towards sustainable nuclear fuel through closed fuel cycles and advance fuel development. This focuses on challenges and issues that need to be addressed for better performance and safety of nuclear fuel in nuclear plants. These focused areas are on development of high conductivity new fuels, radiation induced corrosion, fuel behavior during abnormal events in reactor, and decontamination of radioactive material.

#### **How to reference**

In order to correctly reference this scholarly work, feel free to copy and paste the following:

Yuri Zhukovskii, Dmitry Bocharov, Denis Gryaznov and Eugene Kotomin (2012). First Principles Simulations on Surface Properties and Oxidation of Nitride Nuclear Fuels, *Advances in Nuclear Fuel*, Dr. Shripad T. Revankar (Ed.), ISBN: 978-953-51-0042-3, InTech, Available from: <http://www.intechopen.com/books/advances-in-nuclear-fuel/first-principles-simulations-on-surface-properties-and-oxidation-of-nitride-nuclear-fuels>

# **INTECH**

open science | open minds

#### **InTech Europe**

University Campus STeP Ri  
Slavka Krautzeka 83/A  
51000 Rijeka, Croatia  
Phone: +385 (51) 770 447  
Fax: +385 (51) 686 166  
[www.intechopen.com](http://www.intechopen.com)

#### **InTech China**

Unit 405, Office Block, Hotel Equatorial Shanghai  
No.65, Yan An Road (West), Shanghai, 200040, China  
中国上海市延安西路65号上海国际贵都大饭店办公楼405单元  
Phone: +86-21-62489820  
Fax: +86-21-62489821

© 2012 The Author(s). Licensee IntechOpen. This is an open access article distributed under the terms of the [Creative Commons Attribution 3.0 License](#), which permits unrestricted use, distribution, and reproduction in any medium, provided the original work is properly cited.

IntechOpen

IntechOpen